Dynamics and energetics of a sphere during water exit

Yang Huang (黄扬) ⓘ ; Qing Xiao (肖清) ✉ ⓘ ; Qiang Zhu (朱强) ⓘ

🔴 Check for updates

View Online   Export Citation

Articles You May Be Interested In

Experimental and numerical investigation of the effect of deep-sea mining vehicles on the discharge plumes

Physics of Fluids (March 2024)

Research on cavity collapse characteristics during high-speed water-exit of the supercavitating projectile

Physics of Fluids (July 2023)

Research on launching, water exiting, and river crossing of an amphibious vehicle

Physics of Fluids (November 2023)

Dynamics and energetics of a sphere during water exit

Yang Huang (黄扬),[1] (iD) Qing Xiao (肖清),[1,a] (iD) and Qiang Zhu (朱强)[2] (iD)

AFFILIATIONS

[1]Department of Naval Architecture, Ocean and Marine Engineering, University of Strathclyde, Glasgow G4 0LZ, Scotland, United Kingdom
[2]Department of Structural Engineering, University of California, La Jolla, San Diego, California 92093, USA

[a]Author to whom correspondence should be addressed: qing.xiao@strath.ac.uk

ABSTRACT

By using a multi-phase Navier–Stokes solver combining the volume of fluid approach for water–air interface, the large-eddy simulations method for turbulence effect, and the overset mesh technique for moving boundary, we investigate the dynamics and energetics of a neutrally buoyant sphere during water exit process. The sphere is launched vertically with various initial velocities. In our analysis, the water exit process is divided into three distinct phases, fully submerged, partially submerged, and airborne. The focus is on the roles of the gravity, buoyancy, viscous, and wave-radiation forces in determining the motion and energy exchange/dissipation. During the fully submerged phase, the energy loss of the sphere is caused by the viscous force and the wave-radiation force, with the former playing the dominating role. In the partially submerged phase, the buoyancy force decreases as the submerged volume is reduced. However, under certain conditions, there could be an additional supporting force on the sphere caused by upward water flow beneath it. Once the sphere is fully airborne, its motion is primarily governed by gravity, and the maximum height it attains correlates strongly with the water-exit speed. These findings offer deeper insights into optimizing underwater launch parameters and understanding energy transfer mechanisms in water exit scenarios.

I. INTRODUCTION

The process in which a submerged object ascends through the water–air interface is called "water exit." This process occurs ubiquitously in both natural and engineering activities, e.g., fish leaping out of water,[1,2] underwater projectile launches,[3–10] transitions of unmanned aerial–underwater vehicles from water to air,[11–17] and the retrieval of deep-sea mining vehicles (DSMV).[18,19] Consequently, this problem has attracted significant research interest across various fields.

Water exit is a highly complicated multi-physics problem involving multiphase flows, nonlinear free surface dynamics, turbulence, and cavitation/supercavitation.[4,9,20–23] Existing studies have examined objects with both simple geometries, such as a sphere, an ellipsoid, or a cylinder,[12,24–28] and complex geometries, such as a fish,[1,2] a robotic vehicle,[11] an unmanned aerial–underwater vehicle,[13,29] or a deep-sea mining vehicle.[18,19] These studies concentrate mostly on five key aspects: (a) the dynamic responses of the object, including its kinematics (velocity and displacement) and the forces acting upon it, (b) the development of the entrained water column and free surface deformation, (c) the formation and evolution of cavities attached to the object,

(d) wake formation and vortex structures, and (e) the influence of external conditions, such as floating ice and waves.

Understanding the dynamics of water exit is crucial. Factors such as free surface evolution, the entrained water column behind the object, and the water mass carried by the object continuously act upon it throughout the process. For instance, Takamure and Uchiyama[12,24,30] conducted experiments with solid spheres launched underwater at various depths and initial velocities to explore the relationship between submerged depth and maximum rise height. They also examined the trajectories of spheres with different densities and the deformations of the water surface caused by these spheres. Yun et al.[26] investigated the hydrodynamic characteristics of cylindrical objects during water exit using high-speed photography, focusing on how initial velocity and submerged depth influence the hydrodynamic forces experienced. Ni et al.[31] utilized a boundary element method based on the potential flow theory to simulate the water exit of ellipsoidal bodies, providing detailed data on pressure, force, and progressive free surface deformations. Truscott et al.[32] examined the trajectories of buoyant spheres released underwater. They identified two primary

modes of motion: the vertical mode, characterized by nearly vertical trajectories and larger pop-up heights, and the oscillatory mode, characterized by periodic lateral movements and lower pop-up heights due to unsteady vortex shedding. Tassin et al.[33] numerically modeled the water entry and exit processes of two-dimensional deformable objects. In addition, studies on objects with more complex geometries, such as aerial-underwater vehicles, have also illustrated their dynamic behaviors during water exit.[11,13,14,16,29]

In addition to dynamic responses, several studies have delved into the complex flow phenomena associated with water exit, focusing on entrained water column evolution and free surface deformations. Guo et al.[34] numerically examined the evolution of the entrained water column by partially submerged spheres with various velocities and submergence depths, revealing that the initial submergence depth is a critical factor determining the dynamics and breakup of the water column. Wu et al.[25] employed high-speed cameras to observe free surface motion during the water exit of spheres. Zhu et al.,[35] Greenhow,[28] and Xia et al.[36] analyzed the free surface waves induced by the forced motion of fully or partially submerged horizontal cylinders. Haohao et al.[37] explored the waterfall evolution during the water exit of spheres.

Cavitation during water exit is another focal point. Fu et al.[38] conducted experiments using high-speed cameras to observe the vertical water exit of slender objects. They studied the formation, development, and collapse of surrounding cavities, as well as the dynamic characteristics of shoulder and wake cavities. Similarly, Zhang et al.[3] examined the evolution of cavities during the underwater launch of high-pressure venting vehicles and demonstrated that re-entrant jets were the primary factor influencing cavity development patterns (e.g., partial cavitating and supercavitating states). Moreover, Nguyen et al.,[22] Chen et al.,[4] Zhang et al.,[6] Wang et al.,[7] and Nguyen et al.[9] explored cavitation shedding and collapse phenomena during the water exit of axisymmetric projectiles. They analyzed the pressure profiles during cavitation evolution and elucidated the instantaneous high-pressure phenomena resulting from cavitation collapse. Chu et al.[39] further investigated the evolution of cavities during the water exit of cylindrical bodies and simulated the interactions between the free surface and cavities.

Another prominent research area is the vortex structure around projectiles and underwater vehicles during water exit. Gao et al.[10] utilized delayed detached eddy simulation (DDES) to model the wake of underwater projectiles during launch. Their study provided a detailed analysis of the flow field, vortex structure, and mechanisms of wake vortex evolution. Lin et al.[17] numerically investigated the underwater launch of aerial-underwater vehicles and conducted comparative analyses of wake vortex intensity, pressure distribution, and air–water phase distribution evolution patterns. Likewise, Qu et al.[8] investigated the vortex structures of surface-vented cavities during the water exit of underwater projectiles through numerical simulations.

The impact of floating ice and waves on water exit has also been studied, mostly via numerical modeling. Wang et al.[40] developed a six-degree-of-freedom motion model for floating ice and vehicles using a dynamic fluid–structure interaction (DFBI) module combined with an overlapping grid method. This model was applied to examine how varying ice quantities, thicknesses, and shapes influence cavity evolution and vehicle motion characteristics. Similarly, Zhang et al.,[41] You et al.,[23] and Wang et al.[5] employed coupled computational fluid

dynamics (CFD) and discrete element method (DEM) to study dynamics of underwater and high-speed vehicles, as well as cylindrical bodies, in ice-covered regions. Liu et al.[15] utilized CFD and the VOF method to simulate the stability of aerial-underwater vehicles with different launch angles and velocities at the air–water interface. A similar numerical model was applied by Huang et al.[18,19] to examine the effect of incoming waves on the orientation and motion of deep-sea mining vehicles (DSMV) during water exit.

In summary, most existing studies on the water exit problem concentrate on the kinematics of objects, surface pressure distributions, and the evolution of the surrounding flow field. Meanwhile, detailed analyses of energy exchange and energy loss during this process remains scarce. Understanding the energetics of water exit is crucial because the process inherently involves significant energy conversion and dissipation due to interactions with the surrounding fluid and the free surface. Forces, such as gravity, buoyancy, viscous force, wave-induced force, and surface tension force, affect the energy status of an object and its dynamic behaviors. A comprehensive analysis of how these forces contribute to energy conversion and dissipation can provide deeper insight into optimizing the design of marine vehicles and other systems undergoing water exit.

The paper is organized as follows: First, we describe the physical problem of water exit, dividing the process into distinct stages and defining key parameters. Next, the primary contributions to energy exchange and energy loss during water exit are analyzed. Mathematical formulations, including the governing equations of fluid dynamics, free surface modeling, and numerical aspects, such as the numerical algorithm, computational setup, and overset mesh technique, are then presented. Subsequently, the numerical methods are validated using the water entry problem of a three-dimensional cone. This is followed by the numerical results and discussions regarding the dynamics and energetics of spheres with different initial velocities during water exit. Finally, conclusions are drawn based on the findings.

II. PHYSICAL PROBLEM

As illustrated in Fig. 1, this study investigates the water exit process of a smooth, homogeneous, and neutrally buoyant sphere with diameter D. The sphere is initially positioned at a depth h_0 and launched with an initial velocity U_0. The analysis considers a vertical launch during which the sphere moves along the z axis only, where z is the coordinate in the vertical direction pointing upwards and $z = 0$ is the mean free surface. Driven by its initial velocity, the sphere ascends through the free surface into the air, reaching a maximum height h_1. This process is divided into three phases: phase 1 (fully submerged), during which the sphere moves from $Z = h_0$ to $Z = -0.5D$ (the symbol Z represents the z location of the center of the sphere), phase 2 (partially submerged), during which the sphere moves from $Z = -0.5D$ to $Z = 0.5D$, attaining an exit velocity U_e, and phase 3 (airborne), during which sphere continues upward from $Z = 0.5D$ to its maximum height h_1. In the current study, we consider a case in which $D = 0.2$ and $h_0 = -0.8$ m.

III. ENERGY ANALYSIS

The energy transitions during phases 1 and 2 of the water exit process are the primary focus of this study. Four key factors are considered: (a) gravitational force F_g, which drives the transformation of kinetic energy into gravitational potential energy, (b) buoyancy force F_b, which converts potential energy into kinetic energy, (c) viscosity
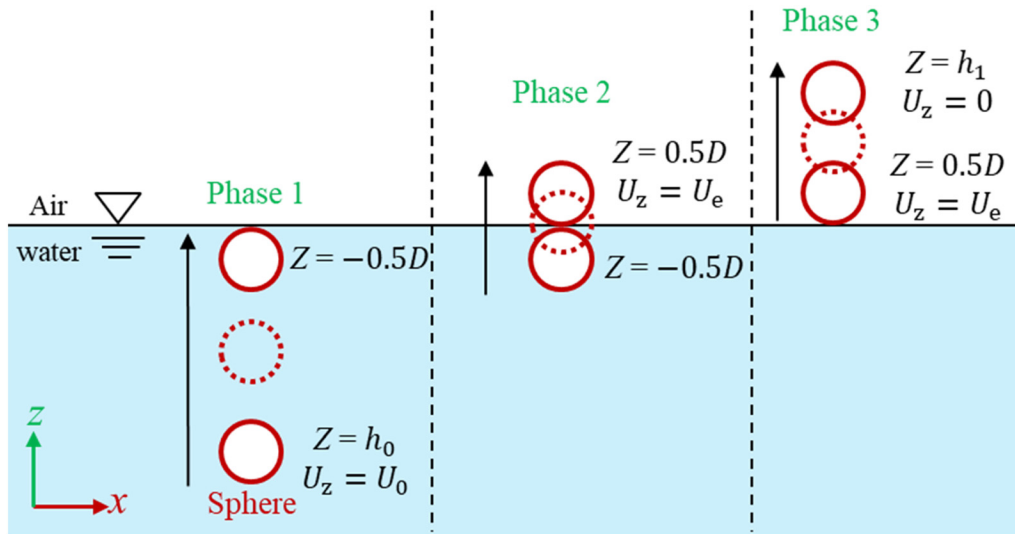
FIG. 1. Schematic of water exit of a sphere.

force F_v, which causes energy dissipation, and (d) wave-radiation force F_w, which results in energy loss through radiation damping. The definition of F_b is based on a linear approximation using the volume of the sphere below the mean free surface $z = 0$. The positive directions of all of these forces are the $+z$ direction.

Incidentally, the above classification of forces is based on their physical origin rather than their directions relative to the motion of the sphere. For example, "drag force," which generally refers to the fluid force opposing the motion of an object, is implicitly represented here as the combination of viscous and wave-radiation forces. Hereafter, symbols with subscripts g, b, v, and w refer to quantities related to gravity, buoyancy, viscosity, and wave effects, respectively.

Although surface tension may play an important role in the dynamics of a sphere as it crosses the water–air interface under certain conditions, the large size of the sphere in this study results in a Weber number (defined as $\rho U^2 D / \sigma$, where ρ is the fluid density, U is the characteristic speed, and σ is the surface tension coefficient) greater than 10. This indicates that the surface tension effects are negligible.

According to conservation of energy, we have

$$E_A + W_g + W_b + W_v + W_w = E_B, \tag{1}$$

where

$$W_i = \int_{z=z_A}^{z=z_B} F_i dz \ (i = g, \, b, \, v, \, w). \tag{2}$$

In Eq. (1), E_A and E_B represent the kinetic energy of the sphere at positions Z_A and Z_B, respectively. W_i ($i = g, \, b, \, v, \, w$) represent the work done by different forces on the sphere.

In phase 1, gravity and buoyancy are balanced (i.e., $F_b + F_g = 0$) so that W_g and W_b cancel each other. The kinetic energy loss during this phase is, thus, purely due to viscous damping and wave radiation damping. In phase 2, when the submerged volume is reduced, $F_b + F_g < 0$. Therefore, during this phase, the reduction in the kinetic energy is caused by the kinetic-to-potential energy conversion as well

as dissipation associated with viscosity and wave radiation. Interestingly, unlike its role as a damper in phase 1 in phase 2 the flow activity associated with the free surface dynamics may actually cause positive energy input into the sphere, a phenomenon further discussed in Sec. VI.

Among the factors influencing the energy state of the sphere, F_g and F_b are well-defined and readily calculated based on the position of the sphere. In contrast, F_v and F_w are coupled, making it difficult to separate their contributions. To address this issue, an approximate method is introduced to decouple the effects of viscous and wave-radiation forces in phase 1.

Toward this end, two simulations need to be performed:

a. The first simulation involves the free ascent of the sphere with initial velocity U_0. In this simulation, the dynamic viscosity of water is $1.0 \times 10^{-6} \, \text{m}^2/\text{s}$, respectively. In this case, the fluid force on the sphere includes contributions from buoyancy (F_b), viscosity (F_v), and wave radiation (F_w). This combined force is calculated and denoted as F_{bvw}.

b. In the second simulation, the sphere follows a prescribed motion based on the displacement time history from the first simulation. However, the viscosity of the fluid is zero so that the dynamic forces on the sphere include the buoyancy and wave effects only. The force obtained this way is, thus, denoted as F_{bw}.

Assuming that the viscous effect does not significantly impact wave generation, the viscous force is estimated as $F_v \approx F_{bvw} - F_{bw}$. Consequently, $F_w = F_{bvw} - F_b - F_v$.

IV. METHODOLOGY

A. Governing equations

CFD simulations are conducted to comprehensively analyze the dynamics of the sphere during water exit, accounting for fluid viscosity, buoyancy, gravity, nonlinear wave–body interactions, and other mechanisms. By employing large eddy simulation (LES), the spatially filtered Navier–Stokes equations become

$$\frac{\partial \overline{u}_i}{\partial x_i} = 0, \quad (3)$$

$$\frac{\partial \rho \overline{u}_i}{\partial t} + \frac{\partial}{\partial x_j}\left[\rho \overline{u}_i\left(\overline{u}_j - \hat{u}_j\right)\right] = -\frac{\partial \overline{p}_i}{\partial x_i} + \frac{\partial}{\partial x_j}\left[\mu_e\left(\frac{\partial \overline{u}_i}{\partial x_j} + \frac{\partial \overline{u}_j}{\partial x_i}\right)\right] - \frac{\partial \tau_{ij}}{\partial x_j}$$
$$+ \rho g_i, \quad (4)$$

where x_i represents the Cartesian coordinates, with the subscript i denoting the ith component, corresponding to the x, y, and z directions (x and y are the horizontal coordinates), respectively. $\overline{u}_i$ represents the resolved filtered velocity component of the flow velocity vector u, while $\overline{p}_i$ represents the resolved filtered pressure. $\hat{u}_j$ denotes the velocity of the moving mesh (see Sec. IV C 3). $\mu_e = \rho(\nu + \nu_t)$ is the effective dynamic viscosity, with ν and ν_t being the kinematic and eddy viscosities, respectively. g_i represents the gravity acceleration.

The subgrid-scale (SGS) stress tensor, $\tau_{ij} = \overline{u_i u_j} - \overline{u}_i \overline{u}_j$, is modeled using the standard Smagorinsky model[42] so that

$$\tau_{ij} = -2\nu_S \overline{S}_{ij}, \quad (5)$$

$$\nu_S = (C_s \Delta)^2 \left(2\overline{S}_{ij}\overline{S}_{ij}\right)^{1/2}, \quad \overline{S}_{ij} = \frac{1}{2}\left(\frac{\partial \overline{u}_i}{\partial x_j} + \frac{\partial \overline{u}_j}{\partial x_i}\right), \quad (6)$$

where ν_S denotes the subgrid viscosity, and the spatial filter $\Delta = (\Delta x \Delta y \Delta z)^{1/3}$ is defined by the grid sizes Δx, Δy, and Δz in the respective directions. The Smargorinsky coefficient C_s is set as 0.14.

B. Free surface modeling

The VOF method[43] is employed to model the interface between water and air. The volume fraction α represents the interface, where $\alpha = 1$ indicates a cell fully occupied by water, $\alpha = 0$ corresponds to a cell filled with air, and $0 < \alpha < 1$ denotes a partially filled cell near the free surface. The evolution of α is governed by the following transport equation:

$$\frac{\partial \alpha}{\partial t} + \frac{\partial}{\partial x_j}\left[(\overline{u}_i - \hat{u}_i)\alpha\right] + \frac{\partial}{\partial x_j}\left[\overline{u}_{ri}(1 - \alpha)\alpha\right] = 0. \quad (7)$$

To maintain a sharp interface and ensure α is conserved and bounded between 0 and 1, an artificial compression term $\nabla \cdot [\overline{u}_r(1 - \alpha)\alpha]$ is introduced. Here, $\overline{u}_r$ is a velocity field that compresses the interface and acts exclusively near the free surface.

The fluid density and viscosity are modeled as a mixture of water and air and expressed as

$$\rho = \alpha \rho_w + (1 - \alpha)\rho_a, \quad (8)$$

$$\mu = \alpha \mu_w + (1 - \alpha)\mu_a, \quad (9)$$

where ρ_w and ρ_a are the densities of water and air, respectively. μ_w and μ_a represent their dynamic viscosities.

C. Numerical issues

1. Numerical algorithm

The fluid solver applies the finite volume method to discretize the governing equations in the fluid domain. Pressure–velocity coupling is implemented using the PIMPLE algorithm, which integrates the

PISO[44] and SIMPLE[45] methods. Temporal discretization is performed using the second-order Crank–Nicolson scheme, with convective terms treated using a second-order upwind scheme. Gradient terms are approximated using a second-order cell-limited Gauss linear scheme.

2. Computational setup

The computational domain, illustrated in Fig. 2, measures $30D \times 30D \times 30D$ in the Cartesian coordinate system, with a water depth of $15D$, where the diameter of the sphere $D = 0.2$ m. As mentioned earlier, the initial position of the center of the sphere is set at $h_0 = -4D$. The sphere maintains a distance of $15D$ from the side walls to minimize wave reflection effects. The sphere has a density matching that of water ($\rho_s = \rho_w = 998.2$ kg/m^3). The range of the initial velocity is $0.75 < U_0/U_c < 2.68$, where $U_c = 3.393$ m/s is the critical velocity required for the sphere to just exit the water (i.e., the highest position of its center is $Z = 0.5D$). The range of Reynolds number (Re) based on the initial velocity and the diameter of the sphere is $5 \times 10^5 < \text{Re} < 4.5 \times 10^6$.

For simplicity, the sphere is only allowed to move along the z-axis. No-slip and no-flux boundary conditions are applied at the side walls and the bottom. A zero-gradient condition for velocity is applied at the top boundary. Boundary conditions are detailed in Fig. 2, where U_z denotes the sphere's vertical velocity.

3. Overset mesh

To mitigate severe mesh deformation caused by significant boundary motions, the overset grid strategy is employed. This technique employs overlapping grids that move independently, enabling the simulation of complex moving geometries without excessive mesh distortion.[46,47]
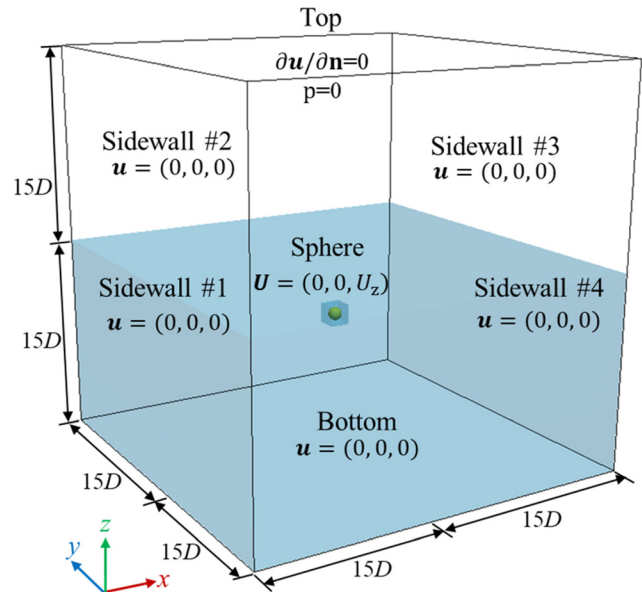

FIG. 2. Computational domain and boundary conditions for water exit motion of sphere.
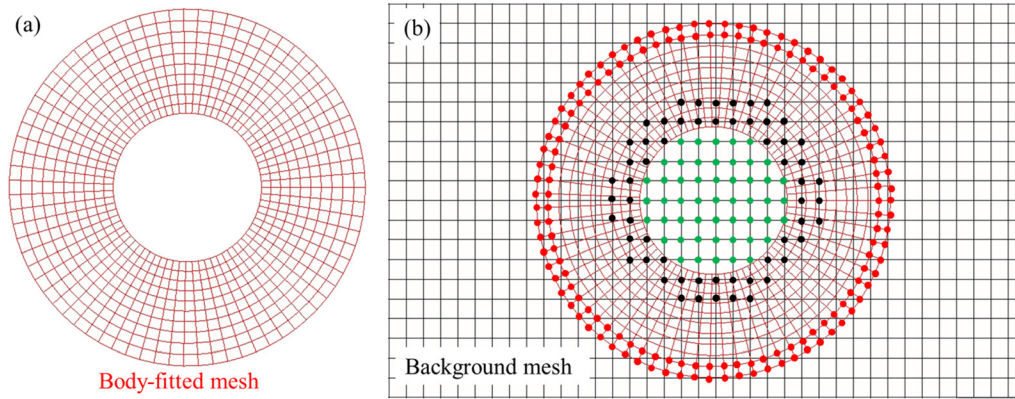
FIG. 3. Schematic diagram of overset mesh: (a) body-fitted mesh and (b) background mesh, where green points represent hole cells, red and black points denote fringe cells, and donor cells are indicated by nearby points.

As illustrated in Fig. 3, our approach uses two distinct meshes: a fixed background mesh, and a body-fitted mesh that moves with the solid object. The background mesh fills the entire computational domain, which remains undistorted throughout the simulation. The body-fitted mesh conforms to the geometry of the moving sphere for high resolution in that critical region. The governing equations are solved on both meshes using the Eulerian framework, and data are exchanged through interpolation between two sets of meshes.

The overset grid workflow consists of four steps performed at each time step:

a. Identification of hole cells: Hole cells are regions in the background mesh that are occupied by the moving body and are excluded from the simulation. These cells are identified and excluded to ensure no fluid equations are solved within them.
b. Identification of fringe cells: Fringe cells, located at the interface between the meshes, enable data exchange between the grids. In the background mesh, fringe cells are adjacent to the hole cells, while in the body-fitted mesh, they are located at the outer boundary.

c. Identification of donor cells: Donor cells are the nearest neighboring cells in each mesh that provide data to fringe cells for interpolation.
d. Interpolation of values between donor and fringe cells: Linear interpolation is used to transfer data from donor cells to fringe cells, ensuring continuity of flow variables across the overlapping grids.

This approach preserves the structure of the background mesh while accommodating the motion of the body-fitted mesh. Although these computations increase the overall cost compared with traditional deforming mesh methods, the overset method provides enhanced flexibility and accuracy for large boundary motions. This makes it particularly suitable for dynamic simulations, such as cross-medium transition.

V. VALIDATION

A. Case A: Water entry of a cone

To validate the accuracy of the numerical method, the water entry of a three-dimensional cone is simulated, and results are compared with experimental data from Lugni et al.[48] As shown in Fig. 4(a), the
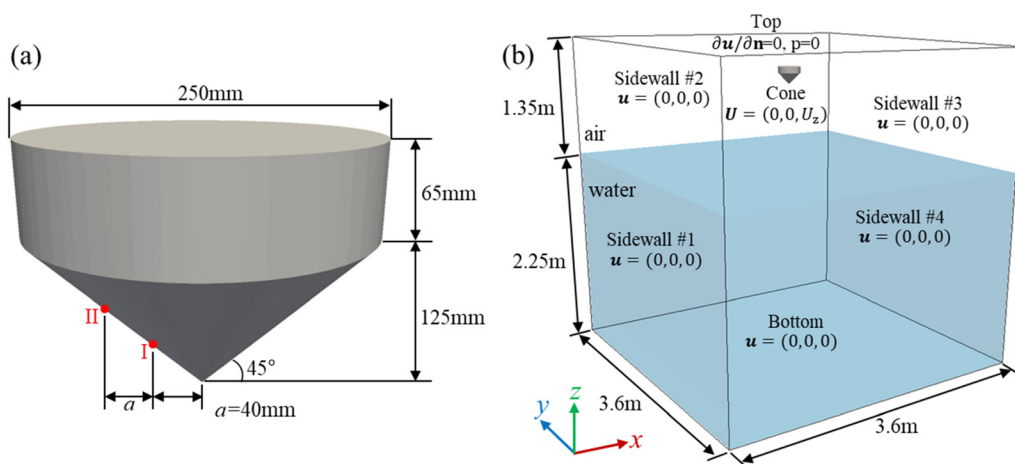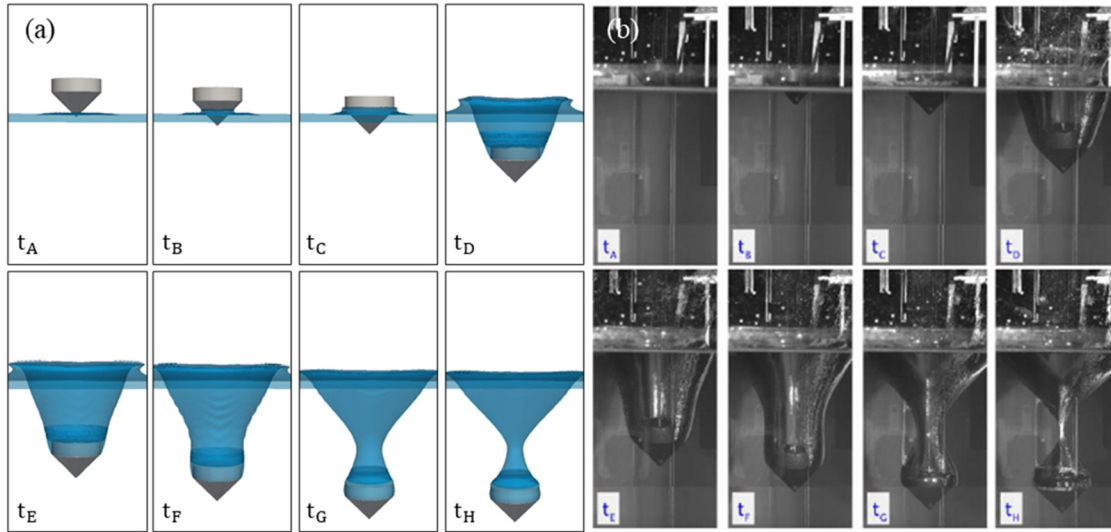

FIG. 4. Computational setup for water entry of the cone: (a) geometry model and (b) computational domain and boundary conditions.

FIG. 5. Comparison of numerical and experimental results for cavity evolution during cone water entry: (a) present work and (b) experiment.[48] Reproduced from Lugni et al., Phys. Fluids **33**(3) (2021). Copyright 2021 AIP Publishing.

cone has a maximum diameter $D_m = 250$ mm, with an upper cylindrical section of 65 mm in height and a lower conical section of 125 mm in height. The density ratio of the cone to water is 1.88. Two monitoring points [I and II, as marked in Fig. 4(a)] are positioned at varying radial distances from the cone's central axis.

The computational domain, shown in Fig. 4(b), measures 3.6 m in length, width, and height, with a water depth of 2.25 m. Initially, the cone is centrally located within the computational domain, with its lower vertex positioned at 1.09 m above the water surface. Starting at rest, it reaches the water surface with a velocity of $3.98\sqrt{gD_m}$, consistent with the experiment. No-slip and no-flux boundary conditions are imposed on the side walls and the bottom, while a zero-gradient velocity condition is applied at the top boundary.

Figure 5 illustrates the evolution of the flow field from the moment of impact to the cavity pinch-off. The left panels present numerical simulation results, where the blue surface represents the free surface, while the right panels depict experimental snapshots. The simulations accurately capture cavity development during water entry, showing reasonable agreement with experimental observations. However, droplet splashing upon cone impact is not reproduced in the simulations, likely due to insufficient mesh resolution.

Figure 6 compares the displacement, velocity, acceleration of the cone as well as time histories of the pressure at the monitoring points between numerical simulations and experimental measurements. Both the dynamic behavior and surface pressure data exhibit good agreement, demonstrating that the current numerical method effectively simulates large boundary motions across the water–air interface.

B. Case B: Flow over a sphere

To further validate the numerical method, simulations of flow over a sphere in a uniform medium were conducted at Re = 3700, where $Re = u_x D/\nu$ is based on the free-stream velocity u_x and the sphere's diameter D. The computational domain is a cuboid region

defined by $x \in [-5D, 20D]$, $y \in [-7D, 7D]$, $z \in [-7D, 7D]$, with the sphere fixed at the origin (0, 0, 0), as depicted in Fig. 7.

At the inlet boundary, an incoming-flow velocity $\mathbf{u} = (u_x, 0, 0)$ is prescribed. The same velocity is applied to all external boundaries except for the outlet, where a zero-gradient condition is imposed. No-slip boundary conditions are enforced on the sphere's surface.

The time-averaged flow characteristics from the present LES simulations are compared with experimental data and direct numerical simulation (DNS) results, as summarized in Table I. The table includes the vortex-shedding frequency (S_t), the separation angle (φ_s) measured from the stagnation point, and the mean drag coefficient ($\overline{C_d}$). Overall, the results show good agreement with previous studies.

VI. RESULTS AND DISCUSSION

This section presents the results on the dynamics and energetics of a sphere with varying initial velocities (U_0) during water exit. The discussion begins with convergence tests for grid size and time step to ensure the accuracy of the numerical simulations. Next, a representative case in which the sphere's initial velocity equals the critical velocity (U_c) is analyzed to provide comprehensive understanding of the dynamic behavior and energy transition during water exit. Subsequently, the results for spheres with varying initial velocities are examined to explore the influence of initial velocity on their behavior throughout the water exit process.

A. Convergence tests

To further ensure the accuracy of the numerical simulations, three sets of grids with different resolutions are generated. The grid size near the sphere and the total number of cells for each set are summarized in Table II. The initial speed of the sphere is set to $U_0 = U_c = 3.393$ m/s. A time step of $\Delta t = 1 \times 10^{-3}$ s is used for this test. In addition, time step independence is examined using $\Delta t = 5 \times 10^{-4}$, 1×10^{-3}, and 2×10^{-3} s with the medium-resolution mesh. Figure 8 shows the time histories of the sphere's displacement
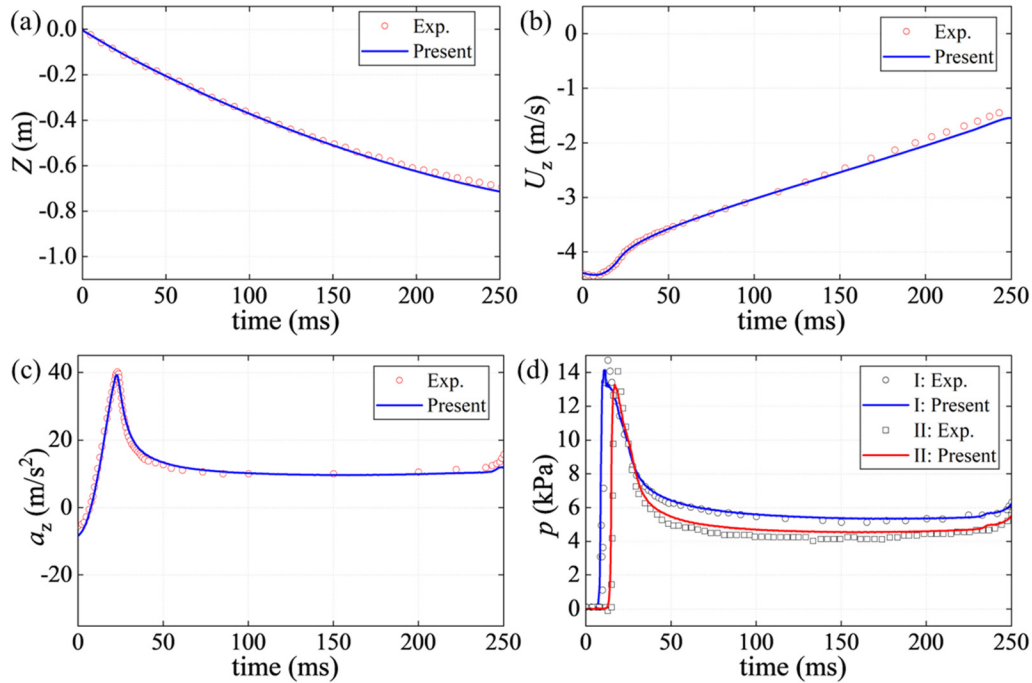
FIG. 6. Comparison of time histories of dynamic behaviors and pressure on the cone after the moment it hits free surface: (a) vertical position of the lower vertex, (b) velocity, (c) acceleration, and (d) pressure.
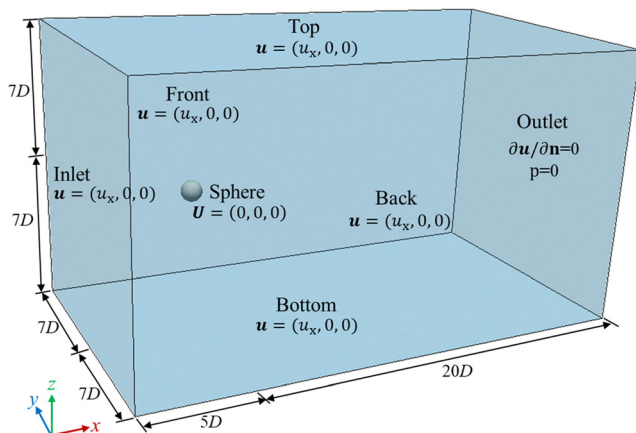

FIG. 7. Computational domain and boundary conditions for flow over a sphere.

TABLE I. Comparisons of dynamic features about the flow around a sphere.

	S_t	φ_s (°)	$\overline{C_d}$
Present work (LES)	0.208	87.8	0.371
Rodriguez et al.[49] (DNS)	0.215	89.4	0.394
Kim and Durbin[50] (exp.)	0.225	$\cdots$	$\cdots$
Sakamoto and Haniu[51] (exp.)	0.204	$\cdots$	$\cdots$
Yun et al.[52] (LES)	0.210	90.0	0.335
Schlichting and Gersten[53] (exp.)	$\cdots$	$\cdots$	0.390

and velocity for different mesh resolutions and time steps. The results indicate that the medium and fine meshes produce similar results, and the results at $\Delta t = 1 \times 10^{-3}$ s closely match those at $\Delta t = 5 \times 10^{-4}$ s. Therefore, to balance computational efficiency and accuracy, the medium mesh with $\Delta t = 1 \times 10^{-3}$ s is selected for subsequent simulations.

B. Dynamics and energetics with critical velocity

1. Dynamic behavior

The kinematic responses of the sphere with critical velocity (U_c) during water exit, including the displacement (Z), the velocity (U_z), and the acceleration (a_z), are first analyzed and presented in Fig. 9.

In phase 1 ($0 < t < 0.421$ s), the sphere remains fully submerged. As it moves upward, U_z decreases due to the effects of viscous force (F_v) and wave-radiation force (F_w), while gravity (F_g) and buoyancy (F_b) remain balanced. As shown in Fig. 10(a), both F_v and F_w are in the opposite direction of U_z, with $|F_v| > |F_w|$. As the sphere approaches the free surface, the magnitude of F_v decreases because it is roughly proportional to the square of U_z. The behavior of F_w is more

TABLE II. Summary of mesh in grid convergence test.

Mesh type	Minimum grid size	Total number of grids
Coarse mesh	$0.049D \times 0.049D \times 0.049D$	1.63×10^6
Medium mesh	$0.035D \times 0.035D \times 0.035D$	4.60×10^6
Fine mesh	$0.025D \times 0.025D \times 0.025D$	13.0×10^6
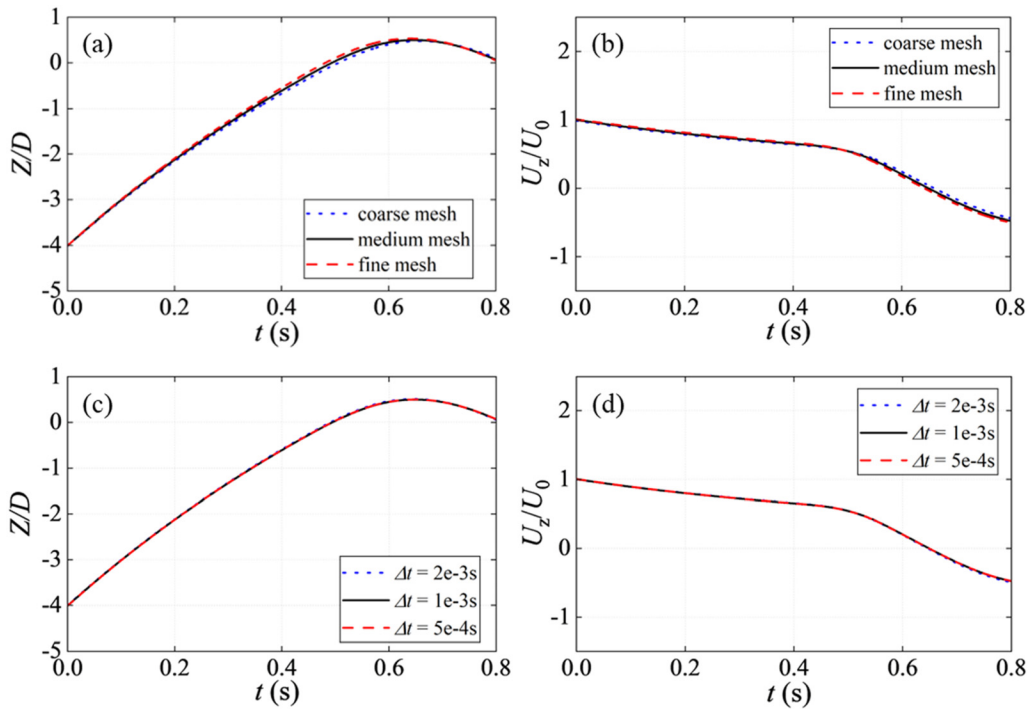
FIG. 8. Time histories of the vertical displacement and velocity of the sphere with different mesh resolutions and time steps: (a) displacement and (b) velocity with different meshes; (c) displacement and (d) velocity with different time steps.

complicated as it is affected by two counteracting effects. On the one hand, as the distance between the sphere and the free surface decreases, the interaction between them increases exponentially. On the other hand, when U_z decreases, the disturbance caused by the sphere on the free surface diminishes, leading to a reduction in the force exerted by the free surface on the sphere. In the specific case shown in Fig. 10(a), the second effect prevails over the first one, and the magnitude of F_w drops as the sphere approaches the free surface. Corresponding to the reduction of the viscous and wave-radiation forces, there is a gradual reduction in $|a_z|$ (see Fig. 9).

In phase 2 ($0.421\,\text{s} < t < 0.657\,\text{s}$), F_b decreases as the sphere begins to exit the water, while F_g remains constant. As gravity exceeds buoyancy, the sphere undergoes rapid deceleration until U_z reaches zero at $0.657\,\text{s}$, when the sphere reaches its highest position ($h_1 = 0.5D$). As the sphere enters air, F_v decreases significantly because of reduced fluid density and viscosity. In addition, in phase 2, there is no easy way to separate F_v from F_w. For simplicity, these two forces are considered jointly as F_{vw}, as shown in Fig. 10(b).

An interesting phenomenon occurs within the time slot $0.6\,\text{s} < t < 0.657\,\text{s}$: although F_b continues to decrease, increasing the disparity between F_g and F_b, the deceleration rate $|a_z|$ does not increase but rather decreases slightly. Further examination shows that this is attributed to the transition of F_{vw} from negative to positive in this stage. Since the viscous force has to remain negative, the implication is that the wave-radiation force begins to act upward [see Fig. 10(b)].

To explore the mechanism behind the negative-to-positive shift in F_{vw} during water exit, the evolution of the free surface is illustrated

in Fig. 11. In phase 1, as the sphere ascends toward the free surface, the water directly above it is not able to flow laterally away quickly enough to accommodate the sphere's upward motion. It accumulates into a dome-like protrusion. As the sphere emerges from water, the free surface is pierced. The water from above the sphere flows downward along its sides and converges below it (Fig. 11 at $Z = 0.25D$). Simultaneously, the free surface on both sides of the sphere sinks below $z = 0$ (indicated by the red arrows), whereas the water column beneath the sphere is raised and provides upward support. This observation offers an intuitive explanation for positive F_{vw} acting on the sphere during this phase.

For insight, the pressure distributions along the sphere's x–z cross section at various instants are illustrated in Fig. 12 to quantitatively explain the transition of F_{vw} from negative to positive. The pressures displayed in the figures are defined as follows:

$$p_s = \begin{cases} \rho g h_w & h_w > 0 \\ 0 & h_w \leq 0, \end{cases} \tag{10}$$

$$p_d = p_t - p_s, \tag{11}$$

where h_w denotes the water depth at the sphere's position (i.e., the vertical distance from the point on the surface of the sphere to the mean location of the free surface, which is equal to the negative of the z-coordinate of this point). Subsequently, p_s is the linearized static pressure on the sphere's surface under the assumption of no free surface deformation. p_t and p_d represent the total pressure and dynamic pressure on the sphere's surface, respectively. Hereby, the total pressure is determined numerically in our model.
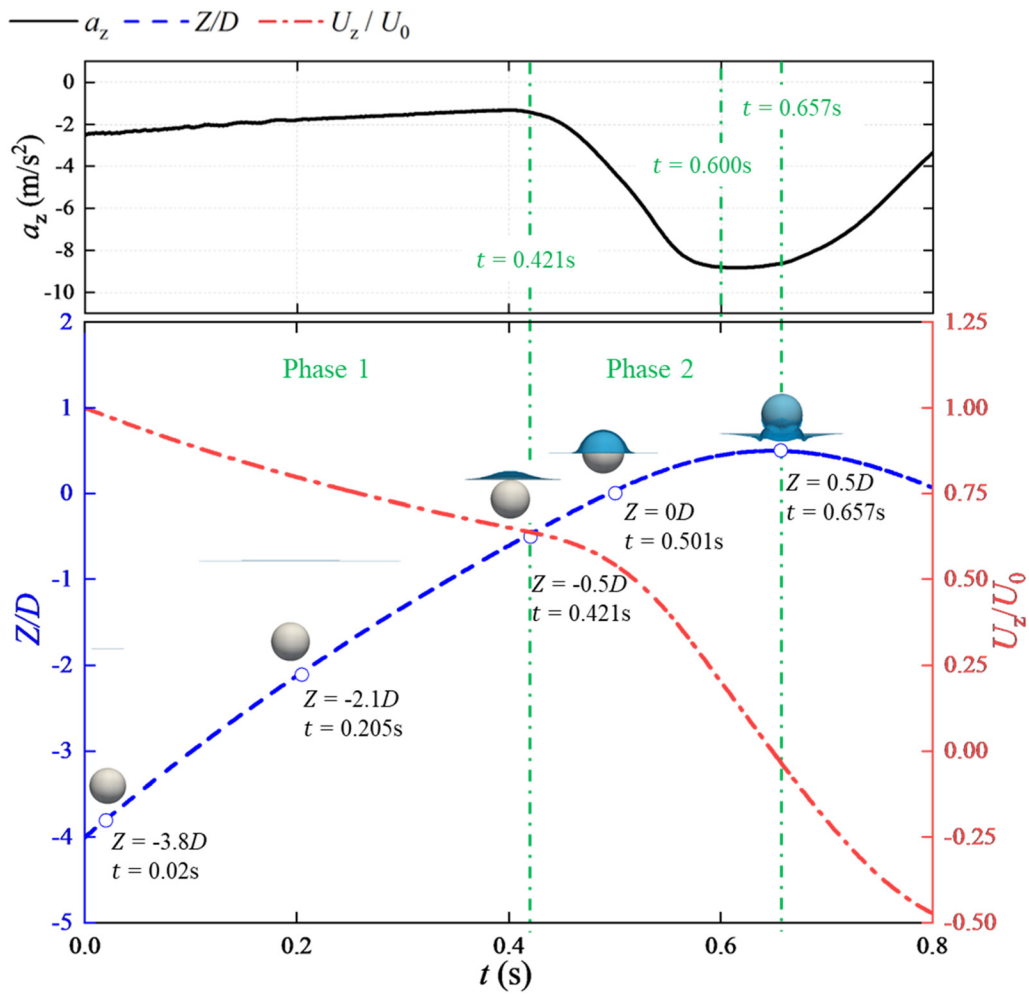
FIG. 9. Time histories of the position (Z), velocity (U_z), and acceleration (a_z) of the sphere with initial velocity $U_0 = U_c$.
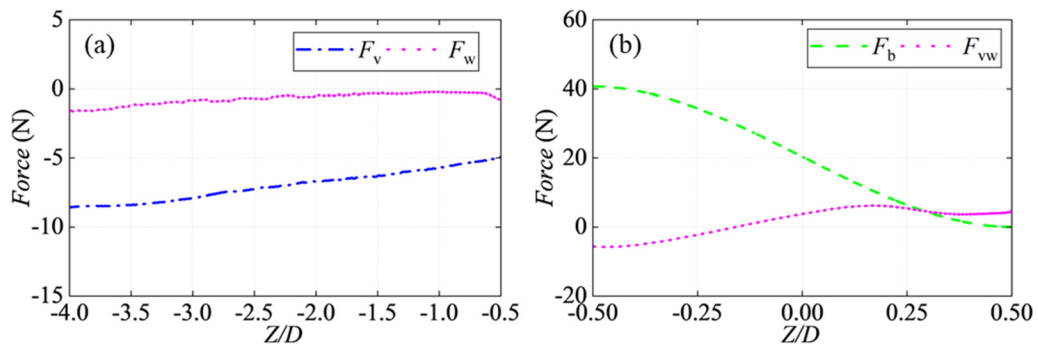

FIG. 10. Variation of external forces acting on the sphere with position: (a) phase 1 and (2) phase 2.
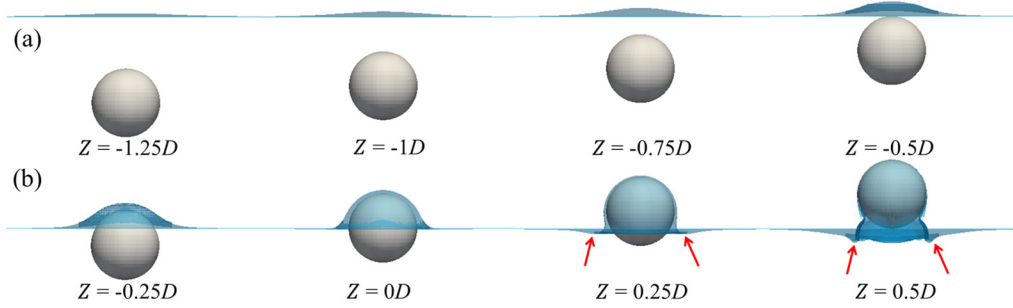
FIG. 11. Free surface at various sphere positions during water exit: (a) phase 1 and (b) phase 2.

The buoyancy force (F_b) acting on the sphere is determined by integrating p_s over the sphere's surface. During phase 2, F_{vw} acting on the sphere includes contributions from pressure effects as well as shear and normal stresses due to viscosity. However, these viscous effects are negligible due to the large Reynolds number (6.8×10^5) so that F_{vw} is mostly attributed to p_d.

As shown in Fig. 12, when the sphere is fully submerged ($-1.25D < Z < -0.5D$), p_s remains positive and is larger on the sphere's lower surface ($-180° < \theta < 0°$) than on its upper surface ($0° < \theta < 180°$), resulting in a positive F_b. During this period, p_d is positive in parts of both the upper surface ($60° < \theta < 120°$) and lower surface ($-150° < \theta < -30°$), with p_d on the upper surface being significantly larger than the one on the lower surface. This leads to a negative F_{vw}, consistent with the results presented in Fig. 10(a).

As the sphere is crossing the free surface ($-0.5D < Z < 0.5D$), its upper surface gradually emerges into the air, reducing p_s to nearly zero, while p_s on the lower surface decreases as it approaches the free surface, resulting in a reduced F_b. Similarly, since the upper surface enters the air, p_d there approaches zero, but p_d on the sphere's lower surface remains positive, driving the negative-to-positive transition of F_{vw}.

Meanwhile, the free surface along the sphere's sides begins to depress, as indicated by the green arrows in Figs. 12(g) and 12(h), causing the surrounding fluid to compress toward the sphere's bottom. This compression increases the positive p_d beneath the sphere to support it.

To gain a deeper understanding of the evolution of the flow field around the sphere during water exit, the velocity field ($u_z - U_z$), pressure field (p_d), and vorticity field are illustrated in Figs. 12–14.

In phase 1, the sphere is fully submerged and surrounded by water. As it ascends, the water above it is pushed, while the water below it moves upward relative to it to fill the void left by the sphere. Meanwhile, water on either side of the sphere moves downward, as depicted in Fig. 13(a). These fluid motions create the dynamic pressure distribution on the sphere's surface: p_d is positive on the upper and lower surfaces, and negative on the sides, as shown in Fig. 14(a). Meanwhile, the downward flow on both sides of the sphere causes flow separation and forms a vortex ring visualized in Fig. 15.

In phase 2, as the sphere emerges from the water, p_d on the upper surface decreases markedly, as illustrated in Fig. 14(b). On the other hand, the water beneath the sphere continues to move upward, forming a jet-like flow beneath it, as presented in Fig. 13(b). This jet provides support to the sphere, increasing p_d on its bottom surface. This explains, more intuitively, the occurrence of positive F_{vw}.

2. Energetics analysis

To investigate the process of energy conversion and dissipation during water exit, the powers of different forces ($\dot{W}_\epsilon$, $i = $ g, b, v, w; hereafter, symbols with dots on top represent time derivatives of the corresponding quantity), as well as the rate of kinetic energy reduction of the sphere ($\dot{E}$), are illustrated in Fig. 16. In phase 2, the power contributions from viscous and wave-radiation forces are considered together and denoted as $\dot{W}_{vw} = \dot{W}_v + \dot{W}_w$.

In phase 1, all forces except F_b do negative work on the sphere, so that $\dot{W}_b$ is positive, while $\dot{W}_g$, $\dot{W}_w$, and $\dot{W}_v$ are negative. Since the magnitudes of $\dot{W}_b$ and $\dot{W}_g$ are the same, they cancel each other. Since $|\dot{W}_v|$ is much larger than $|\dot{W}_w|$, F_v contributes more to the kinetic energy loss than F_w. As the sphere approaches the free surface, U_z decreases, resulting in reductions in $|\dot{W}_i|$ ($i = $ g, b, v, w) and $|\dot{E}|$.

In phase 2, $\dot{W}_b$ gradually decreases until the sphere reaches the peak position ($Z = 0.5D$), where $\dot{W}_b = 0$. $\dot{W}_g$ also approaches zero as U_z decreases. $|\dot{E}|$ initially increases due to the rapid reduction in U_z as F_b diminishes, then decreases as U_z proceeds toward zero. Notably, corresponding to the shift of F_{vw} from negative to positive, $\dot{W}_{vw}$ also becomes positive, indicating that the wave-radiation force does positive work on the sphere.

### C. Dynamics and energetics with different initial velocities

1. Kinematic analysis

To investigate the effect of initial velocity U_0 on the kinematics and energetics of the sphere during water exit, results with various values of U_0 are analyzed. As shown in Fig. 17(a), the maximum height (h_1) reached by the sphere follows an approximately parabolic relationship with U_0. Curve fitting yields the following equation:

$$h_1 = 0.0234(U_0 + 0.0222)^2 - 0.0042 \text{ (m)}. \quad (12)$$

Additionally, as U_0 increases, the ratio of the exit velocity U_e (defined as the velocity of the sphere when $Z = 0.5D$) to U_0 gradually increases, eventually approaching a limiting value of approximately 0.65, as shown in Fig. 17(b). This suggests that the minimum velocity loss during phases 1 and 2 is approximately $0.35 U_0$. Similarly, fitting the relationship between U_e and h_1 yields the following equation:

$$h_1 = 0.0508(U_e + 0.05215)^2 + 0.09856 \text{ (m)}. \quad (13)$$
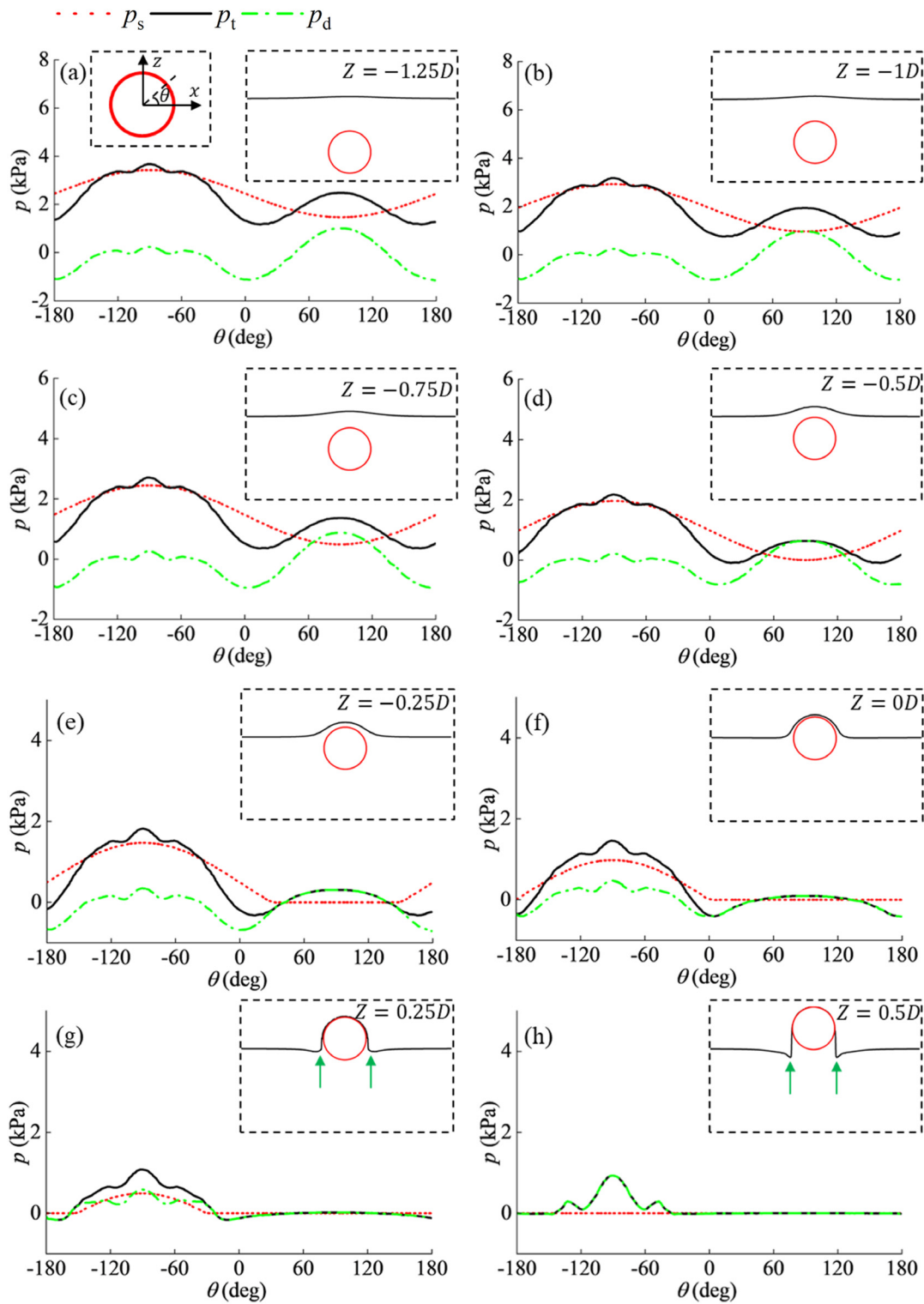
FIG. 12. Pressure distribution on the surface of the sphere within the x–z cross section at various moments: (a) $Z = -1.25D$, (b) $Z = -1D$, (c) $Z = -0.75D$, (d) $Z = -0.5D$, (e) $Z = -0.25D$, (f) $Z = 0D$, (g) $Z = 0.25D$, and (h) $Z = 0.5D$. In the dashed plot in the upper right, the red circle represents the sphere, and the black solid line indicates the free surface.
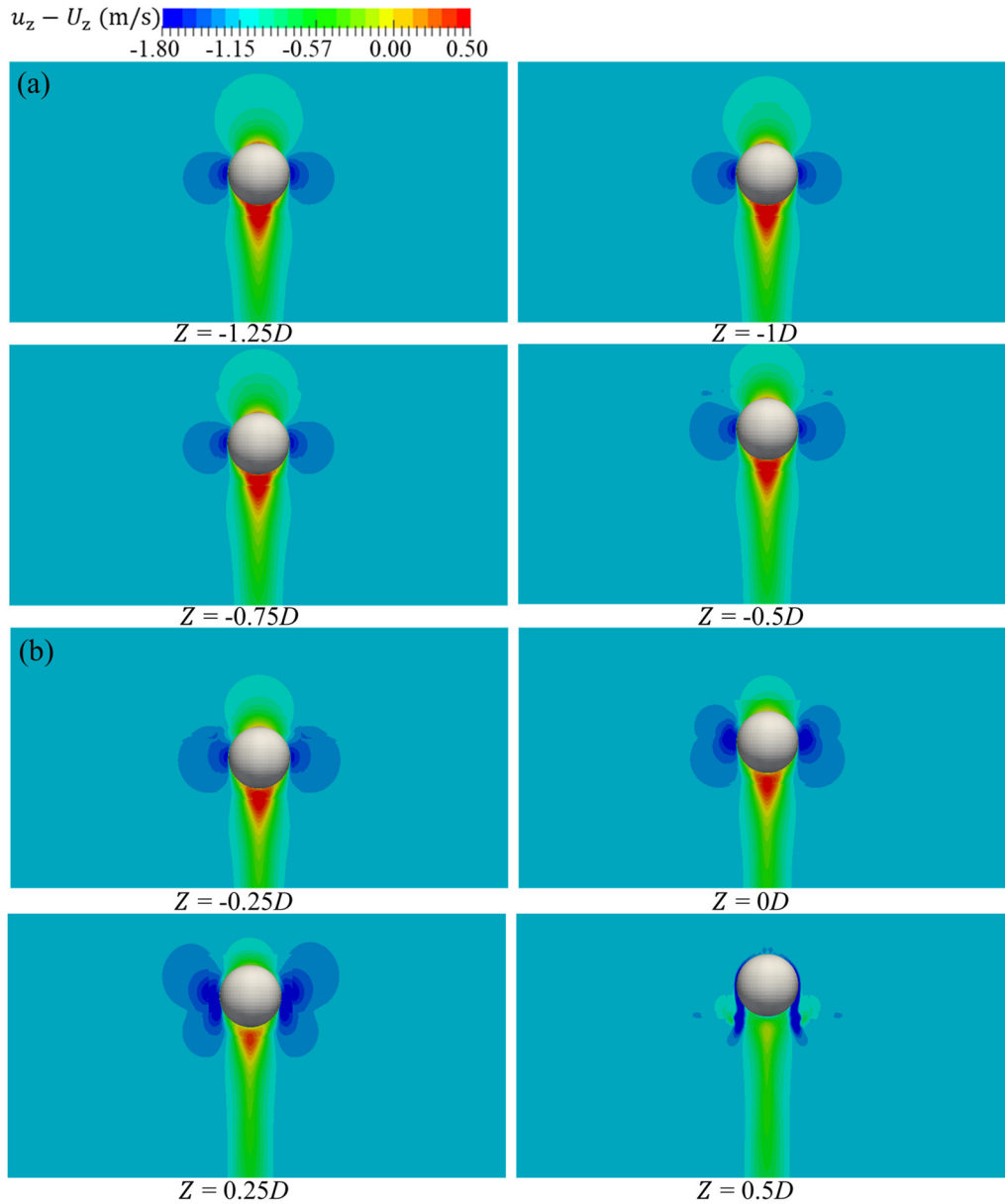
FIG. 13. Relative vertical flow velocity ($u_z - U_z$) around the sphere during water exit: (a) phase 1 and (b) phase 2.

The quadratic coefficient 0.0508 (s^2/m) is close to $1/(2\,g)$, corresponding to the complete conversion of kinetic energy into gravitational potential energy. This indicates that in phase 3 the motion is primarily governed by gravity, while the remaining water jet below the sphere plays a minor role.

2. Energetics analysis

The ratios of the work done by various forces (W_i, where $i = $ g, b, v, w) to the initial kinetic energy (E_0) of the sphere with different initial velocities are shown in Fig. 18. As U_0 increases, these ratios gradually decrease and then plateau. This indicates that the work done by the external forces (F_i, where $i = $ g, b, v, w) becomes proportional to E_0 at larger U_0. As indicated by Eq. (1), $\Delta E = \sum_{i=\text{g, b, v, w}} W_i$, the ratio $\Delta E/E_0$ should also decrease and plateau with increasing U_0. This aligns with the earlier observation that U_e/U_0 approaches a constant at large U_0 [see Fig. 17(b)].

According to Fig. 18(a), in phase 1 all the forces except for buoyancy do negative work. Since gravity (F_g) and buoyancy (F_b) remain constant, and the total displacement in this phase also remains unchanged ($\Delta z = 3.5D$), the work done by gravity (W_g) and that by
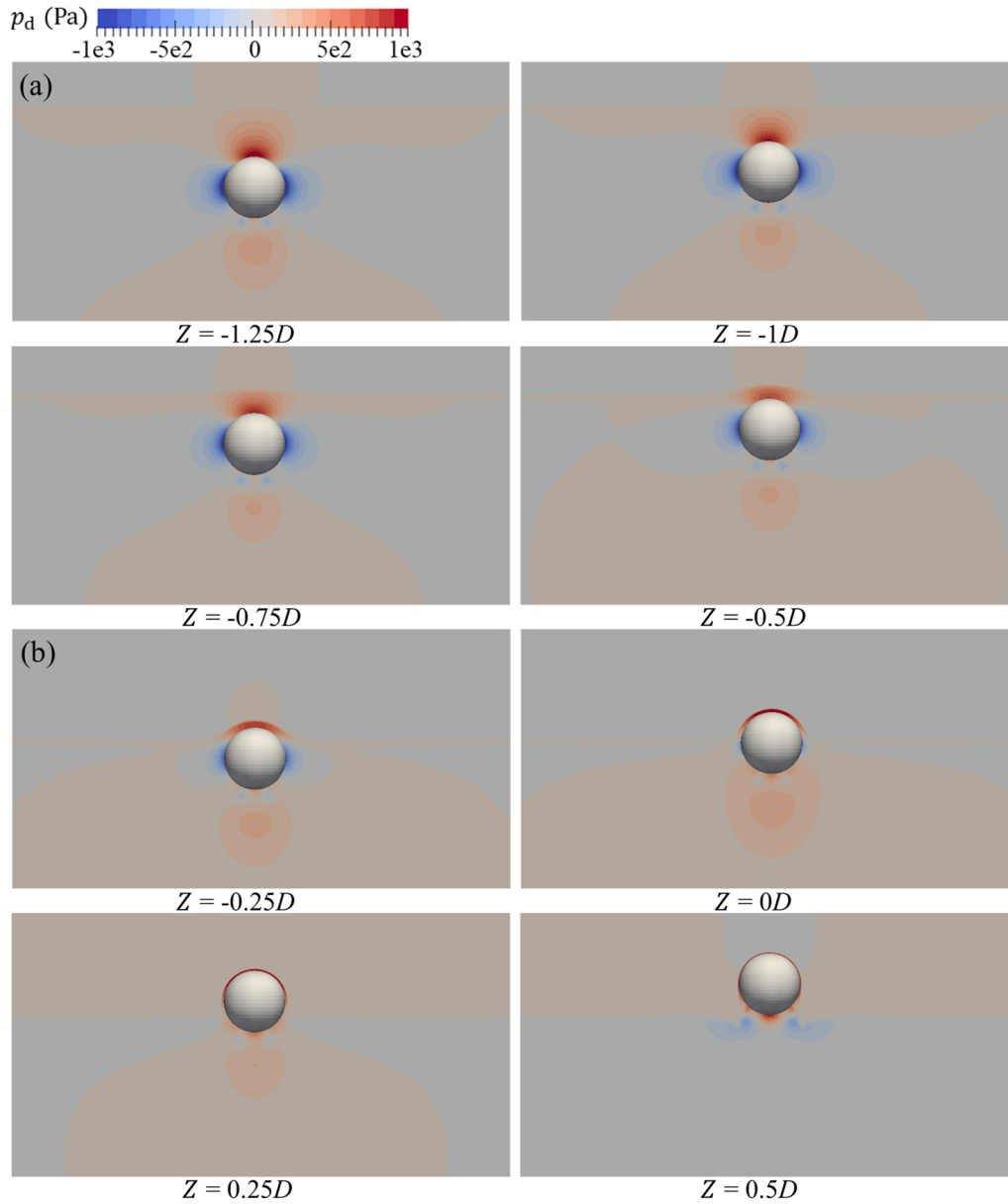
FIG. 14. Dynamic pressure (p_d) field around the sphere during water exit: (a) phase 1 and (b) phase 2.

buoyancy (W_b) are constants. However, as E_0 is proportional to U_0^2, both W_g/E_0 and W_b/E_0 should decrease with U_0. On the other hand, as U_0 increases, both the viscous force (F_v) and the wave-radiation force (F_w) increase, resulting in greater negative work (W_v and W_w), although the ratios W_v/E_0 and W_w/E_0 decrease slightly with U_0 as suggested by our results. Notably, $|W_v|$ is significantly larger than $|W_w|$ within the whole range of U_0 we consider.

In phase 2, W_g and W_b also remain constant, causing W_g/E_0 and W_b/E_0 to decrease with increasing U_0 before approaching zero. Similarly, the work done by F_{vw}, denoted as $W_{vw} = W_v + W_w$, also

decreases as U_0 increases. Interestingly, when $U_0/U_c > 2.01$, W_{vw} shifts from positive to negative. This transition is primarily attributed to changes in the free surface behavior at different initial velocities.

To illustrate this, Fig. 19 shows snapshots of the free surface and the pressure distribution on the surface of the sphere when $U_0/U_c = 2.68$. In this case, the high velocity of the sphere during its passage toward the free surface causes an upward bulge on the free surface. As indicated by green arrows in Figs. 18(g) and 18(h), in this case, there is no downward depression on the free surface for $U_0/U_c = 1.0$ shown in Fig. 12. This implies that during high-speed surface piercing,
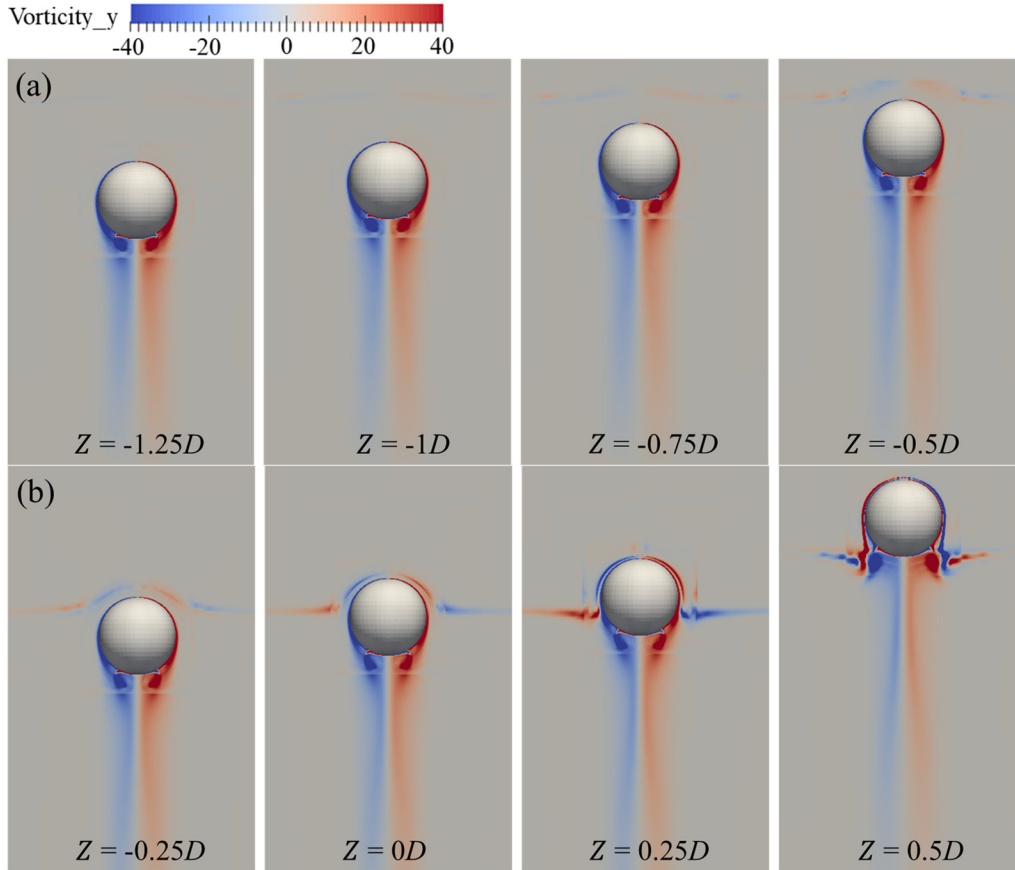
FIG. 15. The y-component of vorticity around the sphere during water exit: (a) phase 1 and (b) phase 2.
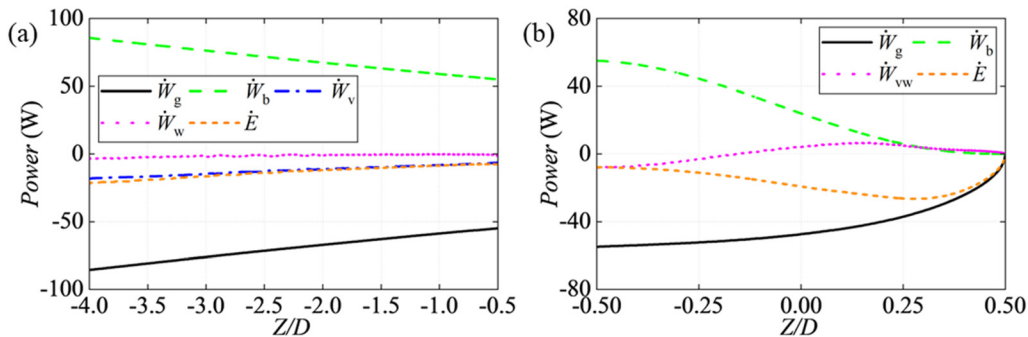

FIG. 16. Power due to external forces on the sphere: (a) phase 1 and (2) phase 2.

a larger region of the sphere remains immersed in water. This leads to significant changes in the distribution of p_d on the surface of the sphere.

Specifically, while p_d on the lower surface ($-150° < \theta < -30°$) remains significantly higher than that on the upper surface ($30° < \theta < 150°$), similar to the case of $U_0/U_c = 1.0$, a notable difference occurs in the lower lateral regions ($-180° < \theta < -150°$ and

$-30° < \theta < 0°$). In these regions, the strong downwash flow induces negative p_d, so that F_{vw} remains negative throughout the water exit procedure, leading to negative W_{vw} in phase 2.

VII. CONCLUSIONS

In this study, a numerical algorithm combining LES and an overset mesh technique is employed to simulate the water exit process of a
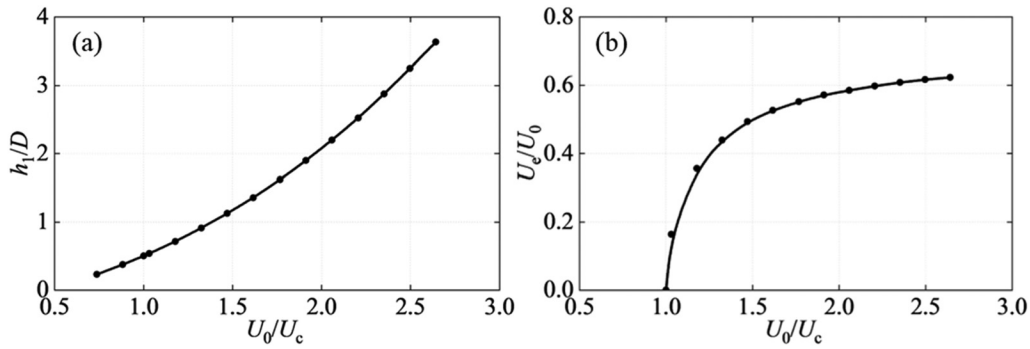
11 February 2025 09:37:37

FIG. 17. Maximum height (h_1) and exit velocity (U_e) of the sphere at different initial velocities: (a) maximum height and (b) exit velocity.
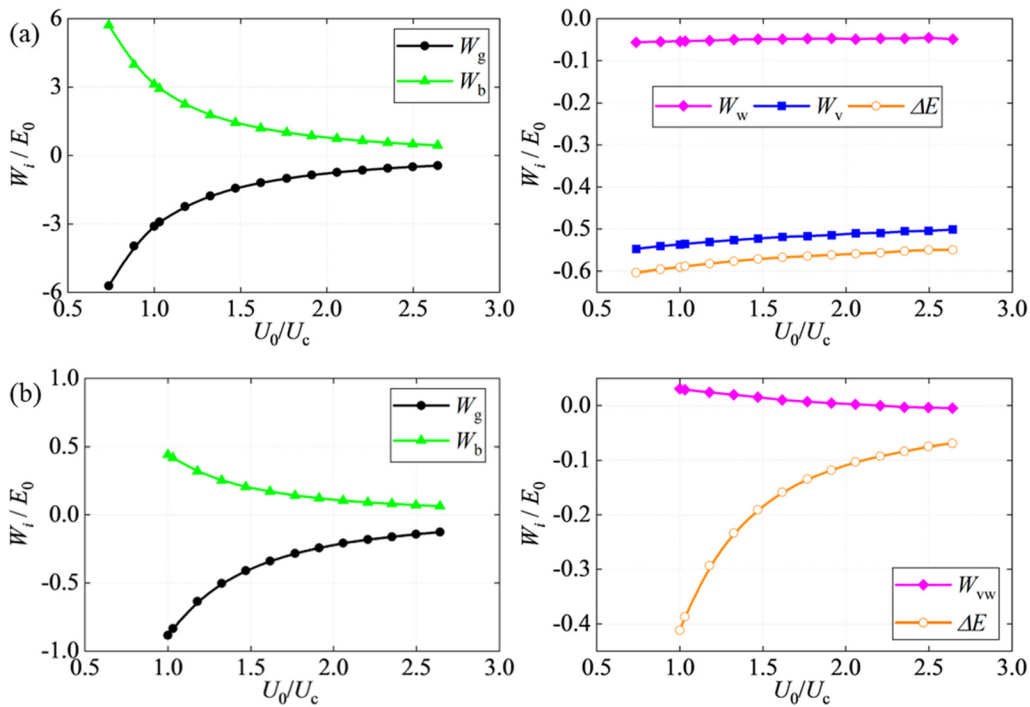

FIG. 18. Work done by various external forces during the sphere's water exit at different initial velocities: (a) phase 1 and (2) phase 2.

neutrally buoyant sphere. The sphere is launched from a fixed underwater position with different initial velocities. The dynamics of the sphere during water exit are then simulated, focusing on its kinematics, flow field evolution, pressure distribution, and energy transitions through gravity, buoyancy, viscosity, and wave-radiation forces. The impact of initial velocity on the kinematics and energetics is also thoroughly examined.

In our study, the water exit process is separated into three phases: phase 1 ($h_0 < Z < -0.5D$), phase 2 ($-0.5D < Z < 0.5D$), and phase 3 ($0.5D < Z < h_1$). During phase 1, gravity and buoyancy forces balance each other, and the kinetic energy of the sphere decreases due to viscous and wave-radiation forces, with the viscous force dominating the process. As the initial velocity U_0 increases, the negative work done by

the viscous and wave-radiation forces relative to the initial kinetic energy of the sphere decreases. The ratio of exit velocity to initial velocity (U_e/U_0) approaches 0.65 as U_0 is increased.

In phase 2, the diminishing buoyancy accelerates the loss of kinetic energy. This energy loss is partially converted into gravitational potential energy and the rest is dissipated through viscous and wave damping effects. Notably, when $U_0/U_c < 2.01$, the wave-radiation force does positive work on the sphere in this phase, which is attributed to the upward jet beneath the sphere. However, this phenomenon disappears when $U_0/U_c > 2.01$.

In phase 3, the sphere is almost fully immersed in air so that buoyancy and wave-radiation effects are negligible. Due to the small viscosity and density of air, viscous force has minimal impact as well.
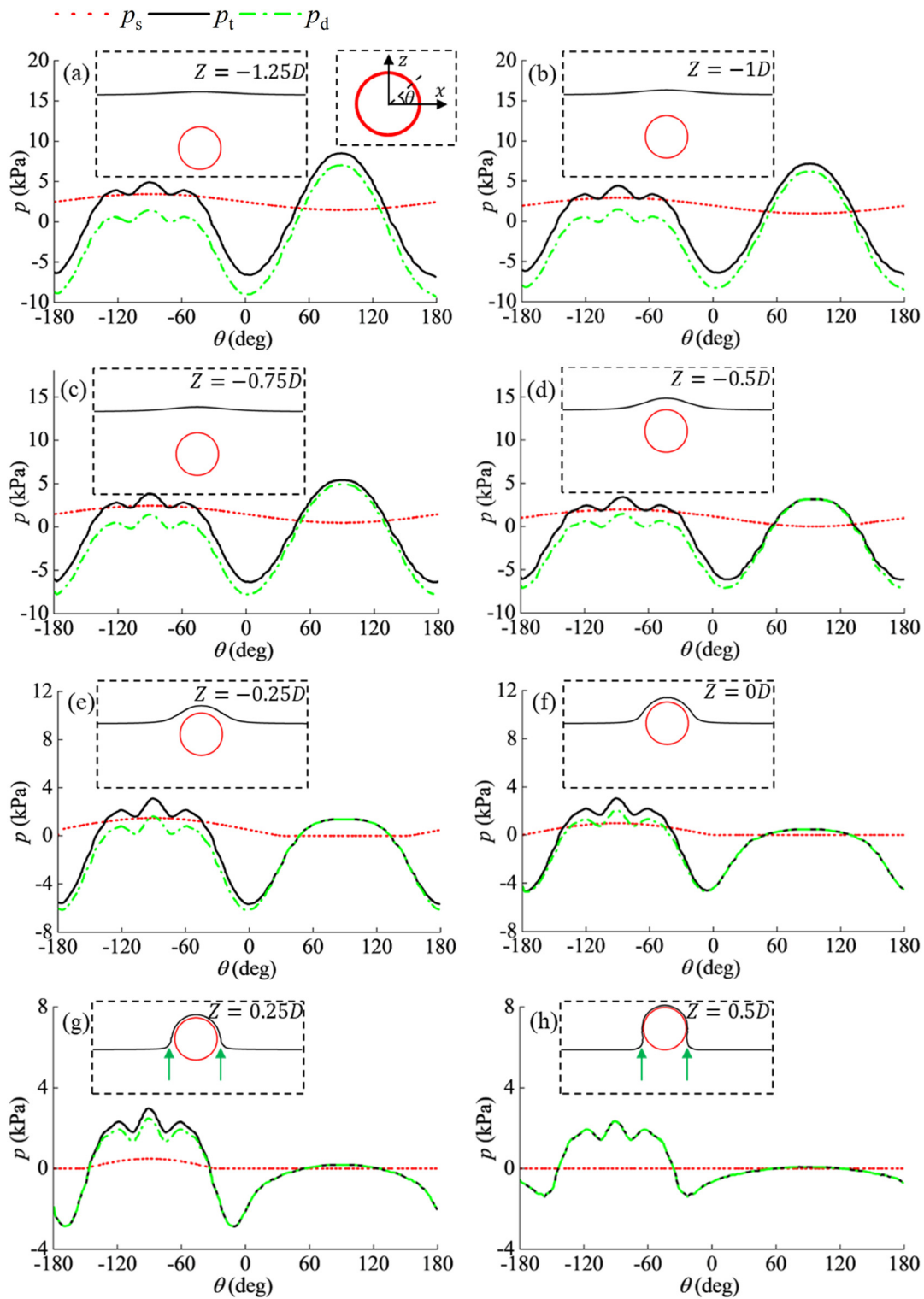
FIG. 19. Pressure distribution on the surface of the within the x–z cross section at $U_0/U_c = 2.68$: (a) $Z = -1.25D$, (b) $Z = -1D$, (c) $Z = -0.75D$, (d) $Z = -0.5\epsilon$, (e) $Z = -0.25D$, (f) $Z = 0D$, (g) $Z = 0.25D$, and (h) $Z = 0.5D$. In the dashed plot in the upper right, the red circle represents the sphere, and the black solid line indicates the free surface.

The dynamics of the sphere is, thus, dominated by gravity. Consequently, its maximum height exhibits a parabolic dependence upon the exit velocity.

This work brings insight about the dynamics and energetics of objects during the water exit process. However, it does not account for factors, such as initial submergence, launch angle, surface tension, and object geometry. Incorporating these factors into future studies could alter the observed energy transfer mechanisms. For example, varying the submergence may change the duration of interaction with water, affecting the acceleration and velocity profiles. Different launch angles could alter flow separation and vortex generation patterns, impacting the hydrodynamic loads on the object. Surface tension becomes particularly important for smaller objects or those with sharp edges. It affects free surface deformation and causes energy dissipation through capillary waves. In addition, objects with certain geometries may generate asymmetric flow fields and pressure distributions, leading to more complicated energy exchange processes.

Understanding these factors is crucial for practical applications, such as the design and optimization of underwater vehicles, projectiles, and marine structures, where accurate predictions of motion, stability, and energy efficiency are essential. Therefore, future research should address these aspects to achieve a more comprehensive understanding of energy related mechanisms in water exit scenarios.

ACKNOWLEDGMENTS

AUTHOR DECLARATIONS
Conflict of Interest

The authors have no conflicts to disclose.

Author Contributions

Yang Huang: Conceptualization (equal); Data curation (equal); Formal analysis (equal); Investigation (equal); Methodology (equal); Software (equal); Validation (equal); Visualization (equal); Writing – original draft (equal); Writing – review & editing (equal). **Qing Xiao:** Conceptualization (equal); Data curation (equal); Formal analysis (equal); Funding acquisition (equal); Investigation (equal); Methodology (equal); Project administration (equal); Resources (equal); Software (equal); Supervision (equal); Writing – review & editing (equal). **Qiang Zhu:** Conceptualization (equal); Data curation (equal); Formal analysis (equal); Investigation (equal); Supervision (equal); Validation (equal); Visualization (equal); Writing – review & editing (equal).

DATA AVAILABILITY

The data that support the findings of this study are available from the corresponding author upon reasonable request.

REFERENCES

[1] V. Saro-Cortes, Y. Cui, T. Dufficy *et al.*, "An adaptable flying fish robotic model for aero- and hydrodynamic experimentation," Integr. Comp. Biol. **62**(5), 1202–1216 (2022).

[2] A. Khosronejad, L. Mendelson, A. H. Techet *et al.*, "Water exit dynamics of jumping archer fish: Integrating two-phase flow large-eddy simulation with experimental measurements," Phys. Fluids **32**(1), 011904 (2020).

[3] Q. S. Zhang, F. R. Ming, X. J. Liu *et al.*, "Experimental investigation of the dynamic evolution of cavity during the free water-exit of a high-pressure venting vehicle," Phys. Fluids **35**(12), 122118 (2023).

[4] Y. Chen, Z. Gong, J. Li *et al.*, "Numerical investigation on the regime of cavitation shedding and collapse during the water-exit of submerged projectile," J. Fluids Eng. **142**(1), 011403 (2020).

[5] H. Wang, Z. Huang, and Z. Guo, "Numerical study on the influence of floating ice on the water-exit hydrodynamic characteristics of a trans-media vehicle," J. Phys.: Conf. Ser. **2478**(11), 112008 (2023).

[6] X. Zhang, X. Lyu, and X. Fan, "Numerical study on the vertical water exit of A cylinder with cavity," China Ocean Eng. **36**(5), 734–742 (2022).

[7] Q. Wang, W. Cao, T. Zhang *et al.*, "Research on cavity collapse characteristics during high-speed water-exit of the supercavitating projectile," Phys. Fluids **35**(7), 073307 (2023).

[8] Z. Qu, J. Cui, X. Chen *et al.*, "Study on vortex structure and hydrodynamic characteristics of water-exit projectile with shoulder ventilation," Ocean Eng. **313**, 119622 (2024).

[9] V. T. Nguyen, T. H. Phan, T. N. Duy *et al.*, "Unsteady cavitation around submerged and water-exit projectiles under the effect of the free surface: A numerical study," Ocean Eng. **263**, 112368 (2022).

[10] S. Gao, Y. Shi, G. Pan *et al.*, "The transient vortex structure in the wake of an axial-symmetric projectile launched underwater," Phys. Fluids **34**(6), 065109 (2022).

[11] R. Zufferey, A. O. Ancel, A. Farinha *et al.*, "Consecutive aquatic jump-gliding with water-reactive fuel," Sci. Robot. **4**(34), eaax7330 (2019).

[12] K. Takamure and T. Uchiyama, "Dynamics of a sphere launched vertically in water," Powder Technol. **372**, 246–257 (2020).

[13] Z. Han, J. Cao, Y. Li *et al.*, "Experimental study on the hydrodynamic of foldable-wing unmanned aerial-underwater vehicles during water-exit process," Ocean Eng. **310**, 118600 (2024).

[14] Q. Zhang, J. Hu, J. Feng *et al.*, "Motion law and density influence of a submersible aerial vehicle in the water-exit process," Fluid Dyn. Res. **50**(6), 065516 (2018).

[15] B. Liu, X. Chen, E. Li *et al.*, "Numerical analysis on water-exit process of submersible aerial vehicle under different launch conditions," J. Mar. Sci. Eng. **11**(4), 839 (2023).

[16] J. Hu, B. Xu, J. Feng *et al.*, "Research on water-exit and take-off process for morphing unmanned submersible aerial vehicle," China Ocean Eng. **31**(2), 202–209 (2017).

[17] W. Lin, H. Xu, T. Sun *et al.*, "Hydrodynamic characteristics of the underwater continuous launching of vehicles under rolling conditions," Phys. Fluids **36**(2), 025130 (2024).

[18] X. Huang, Y. Dai, and X. Zhu, "Numerical study of vehicle motion during water exit under combined lifting force and wave action," Phys. Fluids **36**(10), 107144 (2024).

[19] X. Huang, Y. Dai, C. Liu *et al.*, "Water-exit impact of deep-sea mining vehicles: Experimental and numerical investigations," Ocean Eng. **302**, 117444 (2024).

[20] H. Zheng, H. Qiang, Y. Zhu *et al.*, "Overview of theory, simulation, and experiment of the water exit problem," J. Mar. Sci. Eng. **12**(10), 1764 (2024).

[21] G. Colicchio, M. Greco, M. Miozzi *et al.*, "Experimental and numerical investigation of the water-entry and water-exit of a circular cylinder," in 24th International Workshop on Water Waves and Floating Bodies, 2009.

[22] V. T. Nguyen, C. T. Ha, and W. G. Park, "Multiphase flow simulation of water-entry and -exit of axisymmetric bodies," in *ASME International Mechanical Engineering Congress and Exposition* (American Society of Mechanical Engineers, 2013).

[23] C. You, T. Sun, G. Zhang *et al.*, "Numerical study on effect of brash ice on water exit dynamics of ventilated cavitation cylinder," Ocean Eng. **245**, 110443 (2022).

[24] K. Takamure and T. Uchiyama, "Energy transition in air of a sphere launched vertically upward in water," Ocean Eng. **207**, 107426 (2020).

[25] Q. G. Wu, B. Y. Ni, X. L. Bai *et al.*, "Experimental study on large deformation of free surface during water exit of a sphere," Ocean Eng. **140**, 369–376 (2017).

[26] H. Yun, Q. Liu, Z. Zeng *et al.*, "Experimental study on water-exit of cylinder," Ocean Eng. **293**, 116585 (2024).

[27] B. Y. Ni and G. X. Wu, "Numerical simulation of water exit of an initially fully submerged buoyant spheroid in an axisymmetric flow," Fluid Dyn. Res. **49**(4), 045511 (2017).

[28] M. Greenhow, "Water-entry and -exit of a horizontal circular cylinder," Appl. Ocean Res. **10**(4), 191–198 (1988).

[29] X. Sun, J. Cao, Y. Li et al., "Efficient prediction method for the water-exit characteristics of unmanned aerial–underwater vehicles," Ocean Eng. **302**, 117403 (2024).

[30] K. Takamure and T. Uchiyama, "Effect of density of a sphere launched vertically in water on the water-surface behavior and sphere motion in air," Phys. Fluids **32**(11), 113313 (2020).

[31] B. Y. Ni, A. M. Zhang, and G. X. Wu, "Simulation of complete water exit of a fully-submerged body," J. Fluids Struct. **58**, 79–98 (2015).

[32] T. T. Truscott, B. P. Epps, and R. H. Munns, "Water exit dynamics of buoyant spheres," Phys. Rev. Fluids **1**(7), 074501 (2016).

[33] A. Tassin, D. J. Piro, A. A. Korobkin et al., "Two-dimensional water entry and exit of a body whose shape varies in time," J. Fluids Struct. **40**, 317–336 (2013).

[34] C. Guo, T. Liu, H. Hao et al., "Evolution of water column pulled by partially submerged spheres with different velocities and submergence depths," Ocean Eng. **187**, 106087 (2019).

[35] X. Zhu, O. M. Faltinsen, and C. Hu, "Water entry and exit of a horizontal circular cylinder," J. Offshore Mech. Arct. Eng. **129**, 253–264 (2007).

[36] W. Xia, C. Wang, Y. J. Wei et al., "Experimental study on water entry of inclined circular cylinders with horizontal velocities," Int. J. Multiphase Flow **118**, 37–49 (2019).

[37] H. Haohao, S. Yanping, Y. Jianyang et al., "Numerical analysis of water exit for a sphere with constant velocity using the lattice Boltzmann method," Appl. Ocean Res. **84**, 163–178 (2019).

[38] G. Fu, J. Zhao, L. Sun et al., "Experimental investigation of the characteristics of an artificial cavity during the water-exit of a slender body," J. Mar. Sci. Appl. **17**, 578–584 (2018).

[39] X. Chu, K. Yan, Z. Wang et al., "Numerical simulation of water-exit of a cylinder with cavities," J. Hydrodyn. **22**(5), 834–881 (2010).

[40] H. Wang, Z. Huang, X. Cai et al., "Analysis of the water-exit cavity evolution and motion characteristics of an underwater vehicle under the effect of floating ice," Ocean Eng. **300**, 117374 (2024).

[41] G. Zhang, C. You, H. Wei et al., "Experimental study on the effects of brash ice on the water-exit dynamics of an underwater vehicle," Appl. Ocean Res. **117**, 102948 (2021).

[42] J. Smagorinsky, "General circulation experiments with the primitive equations: I. The basic experiment," Mon. Weather Rev. **91**(3), 99–164 (1963).

[43] C. W. Hirt and B. D. Nichols, "Volume of fluid (VOF) method for the dynamics of free boundaries," J. Comput. Phys. **39**(1), 201–225 (1981).

[44] R. I. Issa, "Solution of the implicitly discretised fluid flow equations by operator-splitting," J. Comput. Phys. **62**(1), 40–65 (1986).

[45] S. V. Patankar and D. B. Spalding, "A calculation procedure for heat, mass and momentum transfer in three-dimensional parabolic flows," in Numerical Prediction of Flow, Heat Transfer, Turbulence and Combustion (Pergamon, 1983), pp. 54–73.

[46] J. L. Steger, F. C. Dougherty, and J. A. Benek, "A Chimera grid scheme," in Advances in Grid Generation, edited by K. N. Ghia and U. Chia (ASME, 1983), pp. 59–69.

[47] S. T. Miller, R. L. Campbell, C. W. Elsworth et al., "An overset grid method for fluid-structure interaction," World J. Mech. **4**, 217 (2014).

[48] C. Lugni, J. Wang, O. M. Faltinsen et al., "Scaling laws for the water entry of a three-dimensional body," Phys. Fluids **33**(3), 036104 (2021).

[49] I. Rodriguez, R. Borell, O. Lehmkuhl et al., "Direct numerical simulation of the flow over a sphere at Re = 3700," J. Fluid Mech. **679**, 263–287 (2011).

[50] H. J. Kim and P. A. Durbin, "Observations of the frequencies in a sphere wake and of drag increase by acoustic excitation," Phys. Fluids **31**(11), 3260–3265 (1988).

[51] H. Sakamoto and H. Haniu, "A study on vortex shedding from spheres in a uniform flow," J. Fluids Eng. **112**, 386–392 (1990).

[52] G. Yun, D. Kim, and H. Choi, "Vortical structures behind a sphere at subcritical Reynolds numbers," Phys. Fluids **18**(1), 015102 (2006).

[53] H. Schlichting and K. Gersten, Boundary-Layer Theory, 7th ed. (McGraw-Hill, New York, 1979) (translated by J. Kestin, Chap. 14 and 20).